CrossMark

ARTICLE

Mesoporous silica beads encapsulated with functionalized palladium nanocrystallites: Novel catalyst for selective hydrogen evolution

Prem Chandra Pandey,[a] Shubhangi Shukla, and Yashashwa Pandey
Department of Chemistry, Indian Institute of Technology (BHU), Varanasi 221005, India

(Received 12 March 2017; accepted 19 May 2017)

2-(3,4 epoxycyclohexyl)ethyltrimethoxysilane (EETMS)/3-glycidoxypropyltrimethoxysilane (GPTMS) mediated, *in situ* synthesis of functional palladium (Pd) nanocomposites over the graphene oxide (GO) surface is reported. The prepared nanocomposites viz, Pd/EETMS, Pd/GPTMS, Pd/GO/EETMS, and Pd/GO/GPTMS, are encapsulated into mesoporous (2–10 nm) silica-alginate beads to primarily serve the development of cost-effective catalyst for on-board generation of hydrogen. Major findings involve: (i) the synthesis of porous silica alginate beads, with the controlled pore sizes (2–10 nm) as a function of concentration of alkoxysilanes, (ii) onboard release of hydrogen from the decomposition of hydrazine, which is evaluated as: (1) time-dependent disappearance of the N–N bond stretching band at 1069 cm^{-1} based on the FTIR spectroscopy, (2) volumetric estimation of the equimolar hydrogen using methylene blue (MB); (3) catalytic reduction of *p*-nitroaniline (PNA). The decomposition of high concentration of hydrazine is made possible using very low concentration of palladium. On calcination the efficiency of catalysts found to enhance further. The noteworthy finding is probing the hydrogen evolution using FTIR spectroscopy. Hydrogen selectivity of ~100% is obtained from the most efficient catalyst (Pd/GO/EETMS-623 K).

I. INTRODUCTION

Hydrogen is considered a requisite energy source for future perspectives, as it is a clean and inexhaustible fuel.[1–3] Besides having an edge over nonrenewable energy resources, efficient storage and utilization of hydrogen is still a challenging task. Recently various technological innovations are done to store the hydrogen energy.[4] Hydrous hydrazine (N_2H_4) which consists of nearly 8.0 wt% of hydrogen, is liquid over a wide range of temperature (298–343 K) and less vulnerable to explosion, therefore, it is considered a promising material for chemical hydrogen storage and transportation.[5,6] Efficient and selective catalysts are required for on-board generation of hydrogen gas from hydrazine. Catalyst reinforced liberation of hydrogen on the decomposition of hydrazine[7,8] is one of the recent major findings. A number of catalysts have been fabricated for the decomposition of hydrazine till date, among them nanoscaled supported catalysts [FeNi/Cu, Ni (100), Ir-MWNTs], nanoparticle catalysts [Pt–Ni (111), Rh (0), Pt (111)] have gained much attention.[9–13] Although these catalysts have been reported to attain 100% H_2 selectivity but almost in every case, decomposition occurred at higher temperature.[14,15] GO-based noble metal nanohybrids[16–18] are helpful in facilitating the dispersibility and electron transfer related issues. The direct growth of nanoparticles over the surface and at the active sites of graphene oxide (GO) prevents the aggregation of nanocrystals and controls the nano geometry.[16–18] However, despite the high catalytic potential of GO based noble metal catalysts, efforts are being applied to either lower the concentrations of noble metal[11] or design noble metal-free catalysts, which are economically viable.

To address these issues, recently the nanocatalysts are entrapped in the polymer matrix of calcium alginate beads, which provide immense dispersibility, and overcome the aggregation related problems which arise specifically due to the high mobility of particles.[19–22] Due to the porous nature of beads, millions of nanoparticles can be enclosed into them. There is a possibility of leaching out of the material since the pore sizes are to the order of 6–16 nm as reported earlier.[19] The pore sizes of such gel beads are not compatible for retaining the nanoscale materials lying between 1 and 10 nm, which limits their operational activity over time.

Here we report the encapsulation of palladium nanocomposites into the silica alginate beads. About 100 ppm concentration of palladium per silica alginate bead effectively decomposes about several thousand folds higher concentration of hydrazine solution (1.19 M), within finite time (~5 s), rendering the silica alginate bead encapsulated with palladium nanocomposites, the cost-effective catalysts for hydrogen evolution. The maximum pore sizes of the calcium alginate beads ranging from 6 to 16 nm,[19] restricts the encapsulation of nanocrystals of 6 and below 6 nm, but the introduction of

Contributing Editor: Xiaobo Chen
[a]Address all correspondence to this author.
e-mail: pcpandey.apc@iitbhu.ac.in
DOI: 10.1557/jmr.2017.226

https://doi.org/10.1557/jmr.2017.226 Published online by Cambridge University Press

 © Materials Research Society 2017

alkoxysilanes into the polymeric matrix of calcium alginate beads due to the specific properties of alkoxy group that allow the formation of –Si–O–Si– linkages within alginate matrix enabling precisely control over the pore size through sol–gel processing.[24] This facilitates the loading of nanomaterials effectively and favors the generation of catalytically efficient silica-alginate mesoporous material. The functional ability of such alkoxysilanes allows the reduction of noble metal ions as reported earlier.[25–28] The palladium nanoparticle suspension homogenized with sodium alginate solution that may permit the formation of mesoporous silica-alginate beads with variable concentration of alkoxysilanes as a result of complex interlocking between both the constituents. The mesoporous structure of silica-alginate beads may further be manipulated by introducing GO, improvements in surface properties led to the enhancement of the catalytic ability of nanocrystallites tailoring the composition of precursors to yield four different types of silica alginate beads namely; (1) Pd/EETMS, (2) Pd/GO/EETMS, (3) Pd/GPTMS, and (4) Pd/GO/GPTMS. Silica-alginate beads loaded with four types of palladium nanocomposites are examined for their catalytic ability toward the decomposition of hydrazine. Kinetics of hydrazine decomposition based on FTIR study justify the decomposition of N–N bond of the same.[29] Almost complete decomposition occurred at room temperature with 100% H_2 selectivity without any appearance of ammonia in the spectra.

Moreover, the amount of hydrogen released is reviewed using simple volumetric measurements, where MB rapidly converts to colourless reduced leuco form i.e., leucoMB on combining with equimolar concentrations of hydrogen gas.[30] Since the hydrogen gas is a reducing agent, thus the hydrogen evolved in the reaction is utilized for the reduction of a nitro compound, *p*-nitroaniline (PNA).[31,32] This also illustrates the rate of the decomposition of hydrazine. Interestingly, these catalysts are also found to potentially catalyze the electrochemical oxidation of hydrazine.[33] Densification of the porous structure of silica-alginate beads occurred through calcinations. Subjection to these alterations may lead to significant improvement in catalytic behavior toward hydrazine decomposition through control over crystallinity of the nanomaterial. The findings on the formation and catalytic behavior of porous silica-alginate beads embodied with GO and EETMS/GPTMS based functionalized palladium nanocrystallites are reported herein.

II. EXPERIMENTAL

A. Materials

Potassium tetrachloropalladate, 3-glycidoxypropyltriethoxysilane (GPTMS), 2-(3,4-epoxycyclohexyl)ethyltrimethoxysilane (EETMS) and polyvinylpyrrolidone (PVP), *p*-nitroaniline, sodium alginate and calcium chloride were purchased from Sigma–Aldrich.

B. Synthesis of gGO and palladium nanoparticles

GO was synthesized using modified hummer's approach. [58]Palladium nanoparticles (PdNPs), Pd/EETMS, and Pd/GPTMS were synthesized using chemical reduction pathway. In the typical procedure, 50 μL of 1 mM solution of K_2PdCl_4, 10 μL of PVP solution was added, followed by the addition of 10 μL of 2.5 M solution of EETMS, the mixture was stirred and incubated for half an hour, brownish black dispersion of Pd/EETMS was obtained. Similarly, the Pd/GPTMS were synthesized using 50 μL of 1 mM K_2PdCl_4 solution, to which 50 μL of GPTMS was added. The mixture was stirred vigorously for 1 min and black colored suspension of Pd/GPTMS was obtained. Similarly, the Pd/GO (Pd/GO/EETMS and Pd/GO/GPTMS) nanocomposites were obtained.

C. Fabrication of beads and doping of nanocrystallites

200 μL of a colloidal dispersion of palladium nanoparticles was mixed with 400 μL of 8 mg/mL sodium alginate solution and sonicated for 30 min till the contents were homogenized. Dissolved 1.9 g of $CaCl_2$ in 20 mL of deionised water, and stirred for few minutes. Then by using a disposal syringe, filled with Pd/GO/alginate mixture, a fast stream was injected into the calcium chloride solution under stirring conditions at room temperature, creating a number of beads. Resulting beads were separated out using fine sieves and washed with distilled water to remove extra calcium chloride and were stored at room temperature for use.

D. Material characterization

Transmission electron microscopy (TEM; Technai G2, 20 TWIN 50/60 Hz 210-240 V, 943205022121, FEI Czech Republic, with accelerating voltage 200 kV) was used to evaluate the morphological features of as-synthesized nanocomposites. Colorimetric analysis has been done using UV spectrophotometer (Hitachi U 2900, Hitachi Corp, Tokyo, Japan). Measurements were done in 1 cm quartz cuvette in the wave length range of 200–600 nm. FTIR analysis was carried out using Bruker, ALFA FTIR Bruker-ATR (Ettlington, Germany) spectrometer. HR-XRD (900 W, 45kV, 200 mA, target-Cu, detector- DTex Ultra 250 with Dtex ultra 250× detector, SMART LAB, RIKAGU Corporation, Akishima, Japan) was used to obtain diffractograms of the materials divulged to higher temperatures. SEM and EDX data obtained with ZEISS EVO 18 Research (Carl Zeiss AG, Oberkochen, Germany).

III. RESULTS AND DISCUSSIONS

A. Synthesis and characterization of palladium nanoparticles

Alkoxysilanes are extensively investigated for their role in the synthesis of nanoparticles in our previous

https://doi.org/10.1557/jmr.2017.226 Published online by Cambridge University Press

reports in the presence of another functional alkoxysilane as reducing agent (GPTMS) or small organic reducing agent [cyclohexanone, formaldehyde, tetrahydrofuran hydroperoxide (THF-HPO)].[25–28] Similarly, other functional alkoxysilanes like EETMS and GPTMS were also studied for their role in casting nanostructured thin film of ormosil.[23] Epoxy linkage present in both these alkoxysilanes are found to be reactive,[34] which facilitates the conversion of metal ion to corresponding nanoparticles. The present process also allows GO stimulated synthesis of PdNPs. Oxygenated functional groups lying on the GO surface are negatively charged which chemically assist the coupling of Pd^{2+} ions with the 2D framework of GO sheets. With the addition of alkoxysilanes as reducing agents, a synergistic co-operation among the functional matrix of GO and organically modified silanes along with the Pd^{2+} ions resulted into clear and stable colloidal dispersions[10,11] of palladium nanocrystallites namely Pd/GO/EETMS and Pd/GO/GPTMS. Figure 1[I(a)] shows the absorbance spectra of Palladium nanoparticles, synthesized using EETMS/GPTMS, in the presence and absence of GO. XPS spectra shown in Fig. 1[I(c)] shows the specific doublet of Pd^0 with peaks $3d_{3/2}$ and $3d_{5/2}$ at binding energies 335.0 eV and at 340 eV respectively. The XPS survey spectrum for all the Pd nanocomposites are reported (Fig. S1).

The results for Pd/GO/EETMS as shown in Fig. 1[I(b)] based on FTIR spectroscopy shows the bands at 3330.6 cm^{-1} due to C–OH stretching of hydroxyl or carboxyl functional groups, 1643.04 and 1016 cm^{-1}

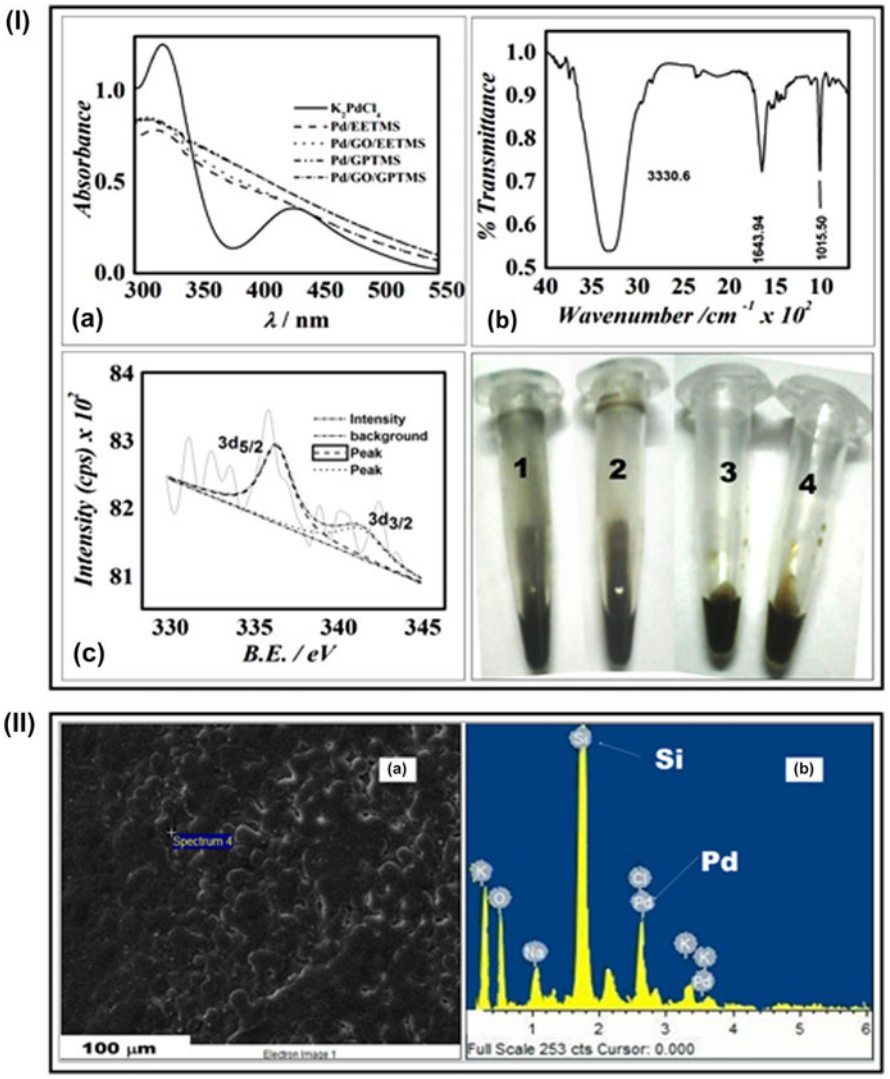


FIG. 1. (I) (a) Absorbance spectra of conversion of Pd^{2+} to Pd^0, (b) FTIR spectra of Pd/GO, (c) XPS spectra of palladium nanoparticles, (d) homogenous suspensions of (1) Pd/GPTMS, (2) Pd/GO/GPTMS, (3) Pd/EETMS and (4) Pd/GO/EETMS. (II) (a) SEM image of dried silica-alginate beads entrapped with nanocomposites and (b) corresponding EDX map showing the distribution of the palladium in the beads along with Si and C.

https://doi.org/10.1557/jmr.2017.226 Published online by Cambridge University Press

correspond to C=O streching and epoxy linkages[35,36] confirmed the presence of oxygen functionalities over the GO surface. Figures 2(I) and 2(II) shows the TEM images, electron diffraction patterns, and the corresponding size distributions of the as synthesized nanocomposites. Pd/EETMS nanoparticles are formed in clusters, as shown in Fig. 2[I(a)], and have an average diameter of 13.4 ± 6.55 nm with broad distribution in particle sizes {Fig. 2[I(e)]}, such diversity in the particle sizes indicates the polydisperse behavior of the particles formed.

On the other hand, the palladium nanocomposites modified with GO i.e., Pd/GO/EETMS {Fig. 2[I(c)]}, are highly reduced in size with an average diameter of 3.41 ± 0.9 nm. This is due to the oxygen functionalities present over the surface of GO which provide the nucleation sites for the nanoparticle growth,[37] controlling the nanogeometry and thus, provides fine dispersibility. Similarly, palladium nanoparticles formed using GPTMS, i.e., Pd/GPTMS are found to be perfectly spherical with an average diameter of 3.8 ± 0.5 nm {Fig. 2[II(a)]}, offering narrow particle size distributions {Fig. 2[II(e)]}. However, in the presence of GO, viz, Pd/GO/GPTMS, despite the homogenous dispersion of the palladium nanocrystals over the graphene surfaces {Fig. 2[II(c)]}, some critical dramatic changes in particle sizes are observed. The average diameter of these nanocomposites (Pd/GO/GPTMS) is observed to be 21.5 ± 7.4 nm {Fig. 2[II(f)]} in contrast to that obtained for the Pd/GO/EETMS nanocomposites. As generated palladium nanoparticles undergo interaction with glycidoxy residue of GPTMS, which may not be allowing GO to show its usual behavior of controlling the nucleation of nanoparticle growth over its surface, resulting in such heterogenity.[38] Further, the TEM images reveal random orientation and angular shapes (viz, cubical, triangular, hexagonal) of Pd/GPTMS nanoparticles and justify the consequence of synthetic procedure adopted during the synthesis. Such multiplicities observed in the nanogeometries of the nanocomposites are one of the factors which decides their differential catalytic behavior in various processes, discussed vide infra in the paper. Selected area diffraction patterns of Pd/EETMS, Pd/GO/EETMS nanoparticles are shown in Figs. 2[I(b)] and 2[I(d)]. The polycrystalline growth of nanoparticles is confirmed from the prominent concentric dotted ring pattern obtained for Pd/EETMS nanoparticles, indexed with the lattice planes (111), (200), (220), and (311) at corresponding *d* values given in Table SI, confirming the fcc arrangement. With the introduction of GO nanosheets in the synthesis of Pd/GO/EETMS nanomaterial,

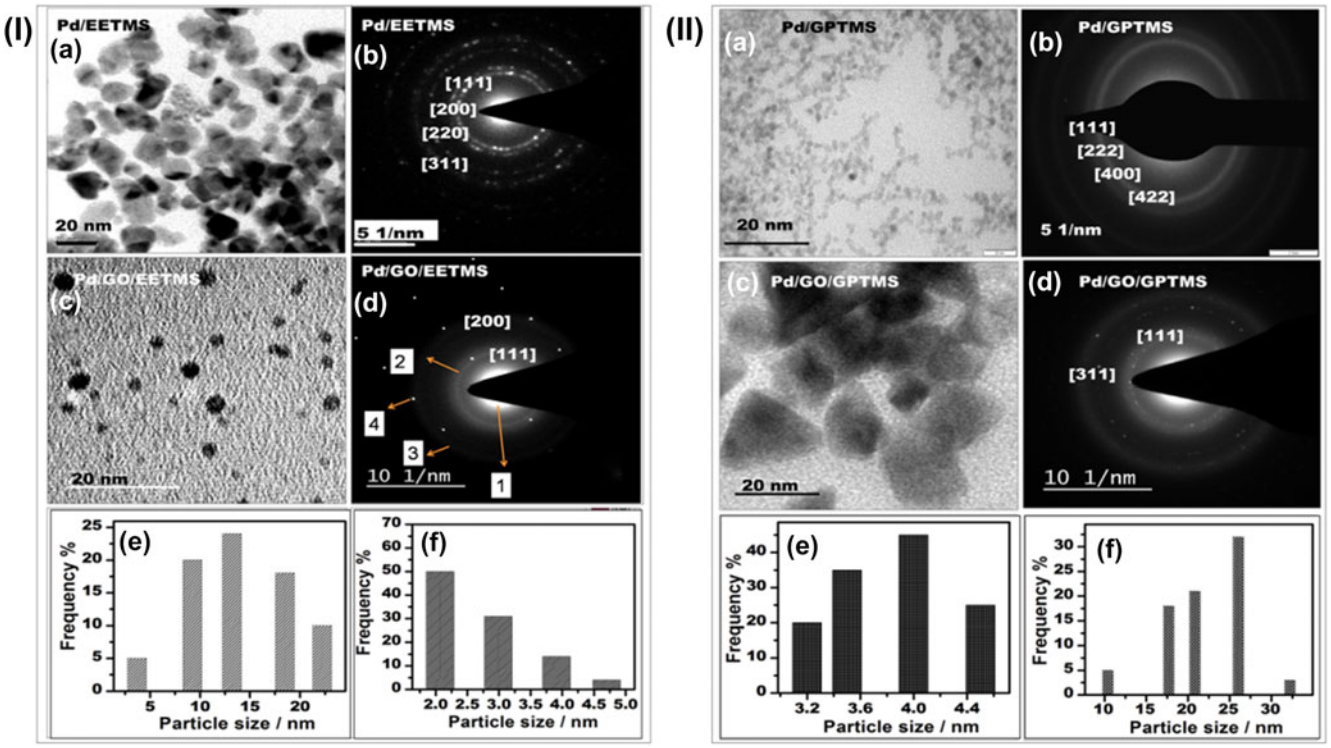


FIG. 2. (I) (a) and (c) TEM images of Pd/EETMS and Pd/GO/EETMS nanocomposites at 20 nm, (b) and (d) descriptive SAED patterns of Pd/EETMS and Pd/GO/EETMS nanocomposites, (e) and (f) corresponding size distributions. The average diameter of (a) Pd/EETMS and (b) Pd/GO/EETMS nanoparticles was 13.4 ± 6.55 and 3.41 ± 0.9 nm respectively. (II) (a) and (c) TEM images of Pd/GPTMS and Pd/GO/GPTMS nanocomposites at 20 nm, (b) and (d) descriptive SAED patterns of Pd/GPTMS and Pd/GO/GPTMS nanocomposites, (e) and (f) corresponding size distributions. The average diameter of (a) Pd/GPTMS and (b) Pd/GO/GPTMS nanoparticles was 3.8 ± 0.5 nm and 21.5 ± 7.4 nm respectively.

https://doi.org/10.1557/jmr.2017.226 Published online by Cambridge University Press

diffractogram shows a specific type of patterns as shown in Fig. 2[I(d)]. It consists of short, medium, and long-range order, along with more than one or two phases. The XRD spectra of Pd/GO/EETMS is reported in Supplementary Material (Fig. S2).

Different features in the SAED pattern are numbered, where 1—white hallow, confirming the presence of a ratio of the amorphous phase of the material. 2 and 3 are diffused rings suggesting the transformation to some degree of poly-crystallization phase 4—white spots confirm the presence of high crystalline phases. The two kinds of lattice planes obtained are (111) and (200) respectively. On the other hand, diffractogram of Pd/GPTMS and Pd/GPTMS/GO are shown in Figs. 2[II(b)] and 2[II(d)] respectively. Polycrystalline nature of the nanoparticles is proved from the complete and focused rings appeared in the electron diffraction image of Pd/GPTMS. These concentric rings are indexed with lattice planes as (111), (222), (400), and (422). The palladium nanocrystals faceted with the lattice planes with corresponding *d*-spacings (Table SI) almost match with that reported in literature. The GO doped nanoparticles (Pd/GO/GPTMS) displayed less defined dotted ring pattern along with the somewhat diffused area in the spectra revealing relatively less crystallinity as compared to that of Pd/GO/EETMS, that contribute to the catalytic activity of as generated nanomaterials.

B. Fabrication and characterization of mesoporous silica alginate beads encapsulated with palladium nanocomposites

Indeed palladium nanoparticles are highly catalytic for most of the operations,[39,40] therefore, it was intended to create a low cost and catalytically efficient material. Calcium alginate polymer matrix has been effectively used for loading zero valent species before.[19] Therefore, we have investigated the possibility of encapsulating the as-made palladium nanoparticles into the porous framework of calcium alginate matrix. Palladium nanocomposite suspensions were found to disperse homogenously in the polymer matrix of alginic acid, which allow their encapsulation to form silica-alginate beads. Presently four types of palladium nanoparticles synthesized in a distinct manner (Pd/EETMS, Pd/GO/EETMS, Pd/GPTMS, and Pd/GO/GPTMS), are encapsulated into the silica beads. The surface properties of these nanoparticle entrapped silica alginate beads are analyzed using Scanning electron microscopy (SEM). The SEM image of the dried silica alginate beads shown in Fig. 1[II(a)], presents a porous three dimensional surface, with interconnected pores. The polymer matrix and the presence of alkoxysilanes as one of the important constituent of the silica alginate beads, favors the formation of an interconnected network of the mesoporous bead. This property facilitates the generation of highly connected pore network, which in turn enhances the surface properties of the beads.

Figure 1[II(b)] shows the corresponding EDX map of Pd/GO/EETMS nanocomposites containing silica alginate beads, displays the distribution of Pd in the ordered framework of beads.

The average pore size of alginate gel beads has been recorded to be 6–16 nm. Exploring such porous dimensions Bezbaruah, et al. (2009) encapsulated iron nanoparticles having average size of 35 nm within the porous alginate matrix for efficient applications.[19] However, the size of as made palladium nanocrystallites lie between 3 and 7 nm, which may not be stable and are likely to leach out from the porous matrix. The choice of applying functional alkoxysilanes in the synthesis of palladium nanocomposites, plays the crucial role in controlling the porous behavior of silica alginate beads via sol–gel processing.[24] Thus the behavior of silica has been evaluated and the role of alkoxysilane concentration during the synthesis of alginate mesoporous beads has been studied. We have investigated the effect of concentration of alkoxysilanes on the porosity of the silica beads, as a function of Si–O–Si linkages and van der Waals interactions between residual groups of polymer and alkoxysilane moieties, which persist at an optimum load of constituents. Figure 3(I) shows the possible chemical interaction between the precursors of the silica-alginate beads, [Fig. 3(II) shows the overview of all the experimental findings]. At lower alkoxysilane content (0.5 M), the embedded colloidal dispersion of nanoparticles leaches out early, due to the less availability of interacting molecules as shown in Fig. S3, weaker communications occur among the respective moieties. On increasing the concentration of alkoxysilanes (2.5 M), resulted in precise control over the compact and flexible character of silica alginate beads.

Figure S3 clearly elucidates the role of silica in the meticulous arrangement of constituting segments, as the spilling out of material from silica beads is the measurement of the extent of interactions thus mesoporous character is achieved with the manipulations in the alkoxysilane content. Optical micrographs shown in Fig. S4 shows the magnified images of the silica beads, at two different concentrations of alkoxysilanes. Figure S4 cites the highly ordered and complicated frame-up of silica bead with smaller pore size, (to the order of 2–10 nm justifying the mesoporous framework suitable for encapsulation of nanoparticles for catalytic applications) in contrast to the one, where the concentrations of alkoxysilanes are low Fig. S4.

C. Decomposition of hydrazine

The decomposition of hydrazine as a function of time was studied over different catalysts. Aliquots collected over fixed intervals of time were scanned within the range

https://doi.org/10.1557/jmr.2017.226 Published online by Cambridge University Press

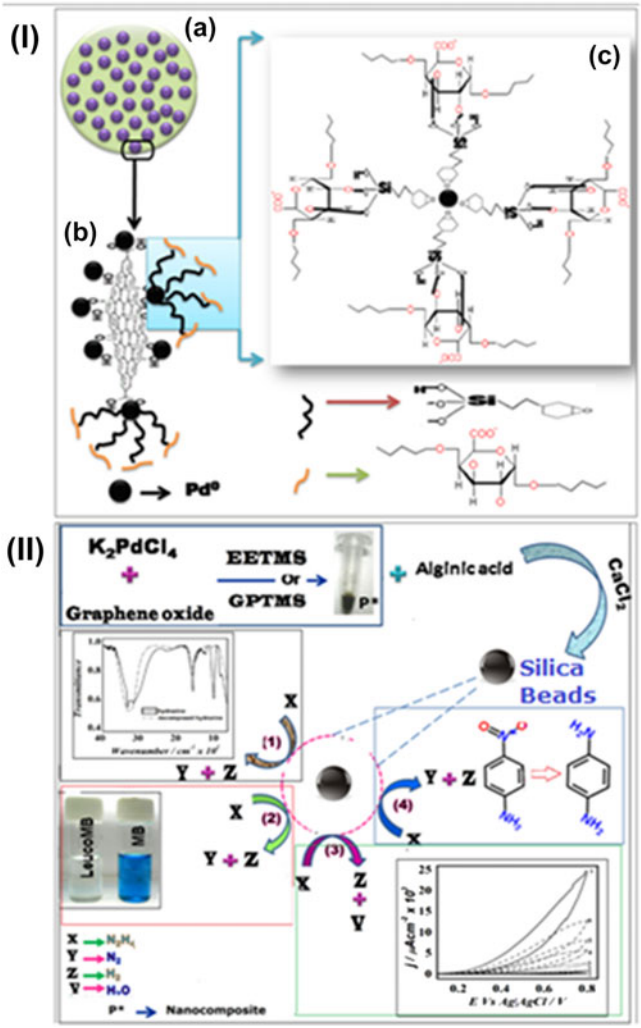


FIG. 3. (I) Pictorial representation of interlinking between alkoxysilanes and polymeric chain of sodium alginate, (a) fabricated silica alginate beads, (b) shows the composition of bead, (c) possible chemical interactions between the precursors. (II) Schematic design of experiment findings on synthesis of silica beads and catalysis, (1) evolution of hydrogen from N_2H_4 on reaction with silica alginate bead as catalysts, (2) conversion of MB to leucoMB in the presence of H_2, (3) electrocatalytic decomposition of N_2H_4 and (4) reduction of p-nitroaniline to p-diaminobenzene.

3600–500 cm^{-1}. Band at 1069 cm^{-1} in IR spectra of hydrazine is due to N–N stretching disappears over time [Figs. 4(a)–4(c)] which indicates the decomposition of hydrazine.[27] The percentage conversion of hydrazine over Pd/GO/EETMS at 623 and 423 K, Pd/GO/EETMS, Pd/GO/GPTMS, Pd/EETMS, Pd/GPTMS at 300 K is obtained as 90–100%, 86%, 80%, 63%, and 45% [Figs. 5(d)–5(e)] over 1 h duration respectively. The decomposition rates were monitored using FTIR spectra. No sign of ammonia was observed in the IR spectra, confirming the complete decomposition of hydrazine into N_2 and H_2. The values of slopes for different $X_{N_2H_4}$%-t curves correspond to the rates of the reaction. The trend of catalytic activity so obtained, follows the order: Pd/GO/EETMS (623 K) > Pd/GO/EETMS (423 K) > Pd/GO/EETMS > Pd/GO/GPTMS > Pd/EETMS > Pd/GPTMS. Heat treated catalysts, i.e., Pd/GO/EETMS is found to be highly active toward the decomposition of hydrazine as compared to others justifying the effect of the surface properties for the activity and selectivity of the catalysts.[15,16] The decomposition of hydrazine is expected to follow the proposed mechanism, reported in Fig. S5 based on the FTIR studies. Pd/EETMS is more efficient than the Pd/GPTMS, because Pd/EETMS has exceptionally better crystallinity properties as clear from the SAED patterns {Figs. 2[I(b)] and 2[II(b)]}, whereas the nanoparticles synthesized using GO are examined to have desirable catalytic activity due to homogenous distribution of the nanoparticles over the graphene surfaces along with the polymeric matrix induced dispersion. In that Pd/GO/EETMS is even faster than the Pd/GO/GPTMS, due to broad differences in their sizes. Later one being bigger in size (~21.5 ± 7.4 nm), as compared to Pd/GO/EETMS (3.41 ± 0.9 nm), are less effective toward the decomposition of hydrazine. Pd/GO/EETMS when treated with elevated temperatures (423 and 623 K), acted as highly potential catalysts with improved efficiencies. Dissolved hydrogen was estimated using methylene blue (MB), as it reacts with equimolar concentration of dissolved hydrogen in solution, and gets converted to colourless reduced form i.e., leucomethylene blue (leucoMB),[29] allowing the convenient assessment of the amount of hydrogen released corresponding to different catalyst added under similar conditions. MB has the absorption maxima at 290 and 662 nm, the band in visible region (at 662 nm) disappears on conversion to leucoform, therefore the reaction dynamics is easily studied by UV–Vis spectroscopy [Fig. 5(a)]. Number of moles of hydrogen evolved (in millimoles) using different catalysts are calculated as: Pd/GO/EETMS-623 K (100), Pd/GO/EETMS-423 K (68), Pd/GO/EETMS (30), Pd/GO/GPTMS (10), Pd/EETMS (1), Pd/GPTMS (0.2) respectively. The results obtained suffice the comparative H_2 selectivity of different catalysts, in the decomposition of hydrazine [Fig. 5(c)].

Figure 5(d) displays the turn over frequencies (TOF) of the corresponding catalysts, which quantitatively defines the activity of the catalyst. The TOF values for different catalysts follow the order: Pd/GO/EETMS (623 K) (300 h^{-1}) > Pd/GO/EETMS (423 K) (270 h^{-1}) > Pd/GO/EETMS (230 h^{-1}) > Pd/GO/GPTMS (180 h^{-1}) > Pd/EETMS (150 h^{-1}) > Pd/GPTMS (80 h^{-1}) respectively.

Present TOF (h^{-1}) values for the decomposition of hydrazine are compared with those of Pt and Ni based catalysts which are good catalysts, yet less efficient than the immobilized catalyst.[29] Further, the kinetic analysis [Fig. 5(b)] inferred that the heat treated catalyst (Pd/GO/EETMS at 623 K) is more efficient.

https://doi.org/10.1557/jmr.2017.226 Published online by Cambridge University Press

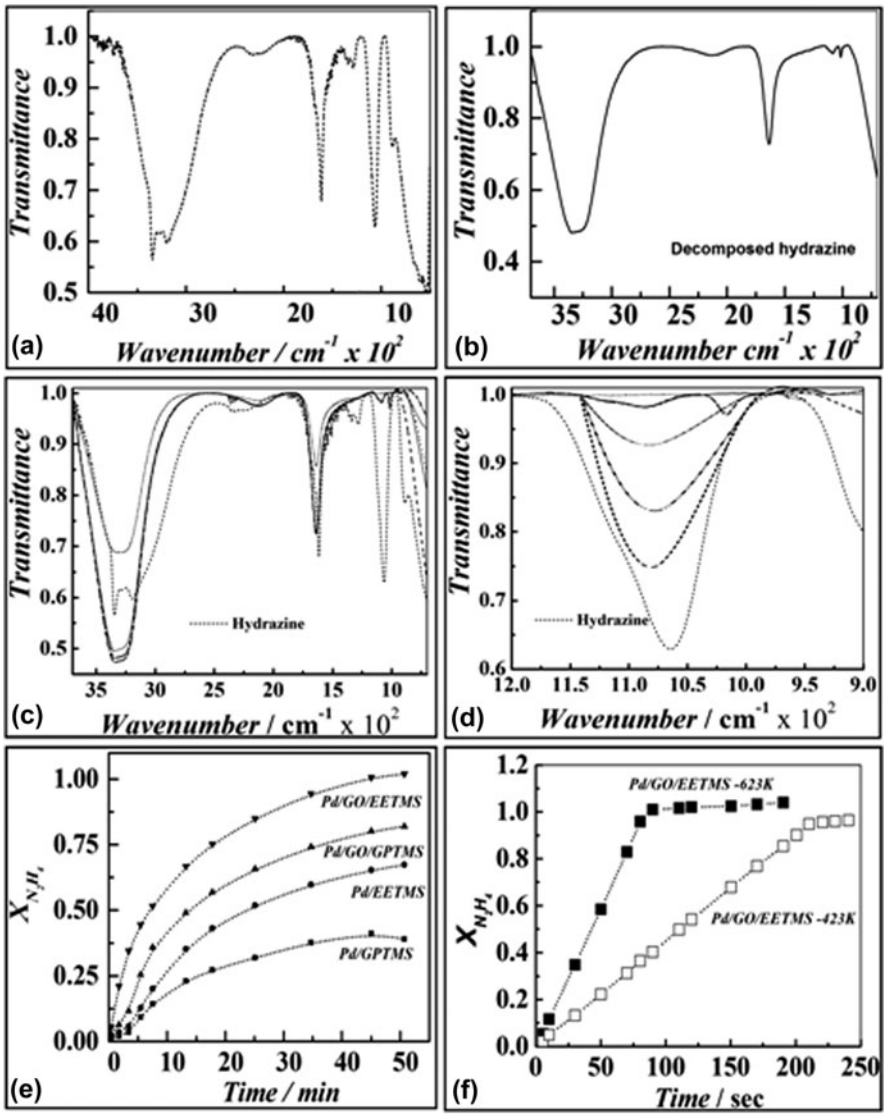


FIG. 4. FTIR spectra of hydrazine solution before (a) and after the decomposition (b), (c) with time degradation of N–N bond stretching, (d) magnified view of the dissipation of the band at 1069 cm^{-1}, (e) and (f) N_2H_4 conversion as a function of time using Pd/GO/EETMS (623 K), Pd/GO/EETMS (423 K), Pd/GO/EETMS, Pd/GO/GPTMS, Pd/EETMS, Pd/GPTMS catalysts at initial hydrazine concentration of 1.19 M.

The silica alginate bead encapsulated palladium nanocomposites are used as effective heterogenous catalysts for the evolution of hydrogen in the reduction of *p*-nitroaniline (PNA).[30,31,44,45] The absorbance maxima of PNA lie at 400 nm and on reduction to *p*-diaminobenzene, it is shifted to 310 nm, this blue shift in wave length can be monitored conveniently. Relative rates of reduction reactions for all the catalysts (Pd/EETMS, Pd/GO/EETMS, Pd/GPTMS, Pd/GO/GPTMS) are recorded using UV–Vis spectroscopy as shown in Fig. 6(I).

The slopes of the plots of natural logarithm of the variations in absorbance against time, yields apparent rate i.e., k_{app}. At regular intervals the absorbance was recorded (A_t, absorbance at different periods, while A_0 is initial absorbance) and the graphs were plotted, from where slope was obtained (k_{app}). The rate constants were calculated at 298 K for Pd/GO/EETMS, with and without heat treatments. The values of slopes are 0.271 min^{-1} (4.5×10^{-3} s^{-1}) 0.428 min^{-1} (7.1×10^{-3} s^{-1}), and 1.03 min^{-1} (17.1×10^{-3} s^{-1}) for Pd/GO/EETMS, Pd/GO/EETMS (423 K), and Pd/GO/EETMS (623 K) respectively in comparison to the earlier reports where Pt (4.6×10^{-4}),[41] Au/PMMA ($7.2–7.9 \times 10^{-3}$),[42] PAA/Ag (0.3 ± 0.1).[43] The highest value of slope is obtained for Pd/GO/EETMS (623 K), which is comparable to the values calculated so far for Pd based catalysts.

Absorbance spectra were recorded with the subjection of catalysts and hydrazine (100 μL, 1.19 M), using the aliquots from the undergoing reactions. The reactions

https://doi.org/10.1557/jmr.2017.226 Published online by Cambridge University Press

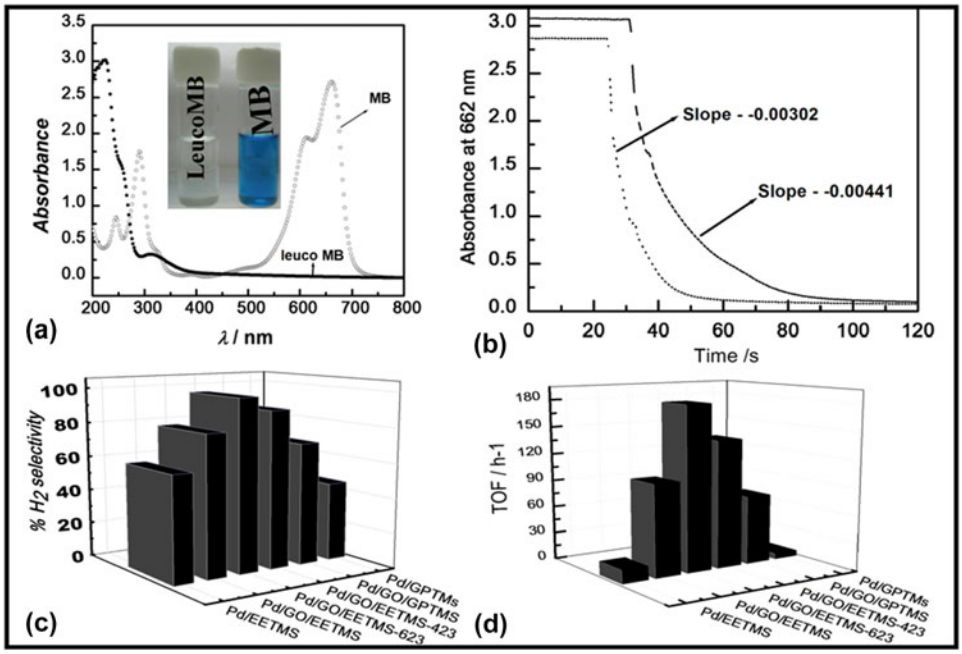


FIG. 5. (a) Absorbance spectra of the reduction of methylene blue (MB) to leucomethylene blue (leucoMB), (b) kinetic analysis of the process without (1) and with (2) temperature treatment of catalyst, (c) comparative hydrogen selectivity's, (d) TOF on decomposition of hydrazine by different catalysts, Inset to (a) shows the change in color at the end point.

took 65, 40, 30, 10 min in case of Pd/GPTMS, Pd/EETMS, Pd/GO/GPTMS, and Pd/GO/EETMS as evident from the bar diagrams [Fig. 6(II)] representing the variations in absorbance relative to time. Basis of these deviations are the same, as explained earlier. The fine pore sizes of the silica beads encapsulated with Pd/GO/EETMS nanocomposite, lead to the fast interaction with the PNA molecules, resulting in the rapid chemical change. The order of the catalytic aptitude achieved is Pd/GO/EETMS > Pd/GO/GPTMS > Pd/EETMS > Pd/GPTMS.

D. Stability and recyclability studies

Silica-alginate beads before and after heat treatments are compatible to recycling, i.e., these can be regained from the reaction mixture and can be applied to another cycle of experiments, hence they are highly cost effective. These are found to retain, splendid catalytic potential irrespective of being used in a recurring manner for successive set of operations.

Figure 6[IV(c)] shows the efficiency of the catalyst (silica alginate bead with Pd/GO/EETMS nanocomposite) used over 4–5 experimental cycles. Appreciable activity of the catalysts was observed over successive cycles, retaining about 80% of its activity even after 5 cycles, which defines its fair catalytic accessibility.

The same catalyst was studied for its stability toward the release of hydrogen and in turn reduction of nitro compound (PNA) over 5–6 days. Figures 6(a)–6(b) shows the similar activity after 5–6 days.

E. Electrocatalytic oxidation of hydrazine

The electrochemical oxidation of hydrazine was studied over all the catalysts reported here. Electrochemical measurements were performed by cyclic voltammetry (CV) on a glassy carbon electrode. The CVs of the different catalysts toward hydrazine oxidation are depicted in Fig. 7(I). Very slow oxidation was observed in the presence of 50 mM without catalyst introduction. All the catalysts showed subsequent increase in current with the oxidation occurring between 0.3 and 0.5 V. A significant rise in current in the presence of Pd/GO/EETMS validates that Pd/GO/EETMS is more efficient over others [Fig. 7(I)]. The maximum current density obtained is about 20–25 mA/cm^2 at potential of 280 mV which is much higher than that obtained with electropolymerized electrode modified with AuNPs and PtNPs (45 μA).[41]

F. Effect of heat treatment

The technology of encapsulation of nanomaterials into the silica alginate beads further extends the possibilities of their conversion to highly competent materials for catalysis. The advantages of such transformations include the modification of the colloidal dispersion of palladium nanoparticles into the even more, dynamic configuration, accountable for its wider access toward high catalytic activity. On the other hand, it is immensely challenging and arduous technique to remodel the colloidal dispersion of palladium nanoparticles into powdered palladium metal profile, as their treatment at elevated temperatures generally mutates the nano-geometry.

https://doi.org/10.1557/jmr.2017.226 Published online by Cambridge University Press

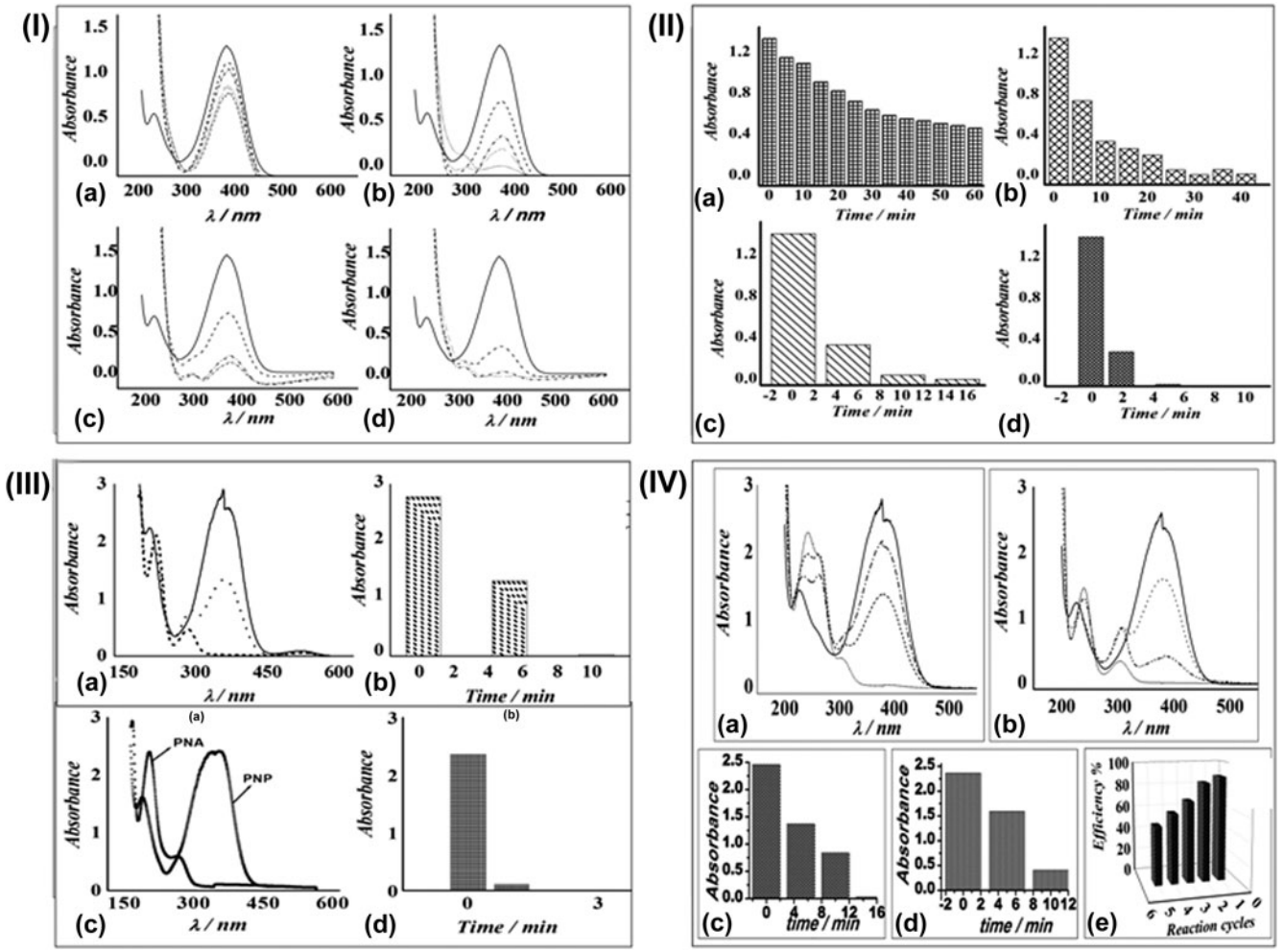


FIG. 6. (I) Absorbance spectra of *p*-nitroaniline reduction using (a) Pd/GPTMS, (b) Pd/EETMS, (c) Pd/GO/GPTMS, and (d) Pd/GO/EETMS. (II) Bar diagrams representing the variation in absorbance and completion of reaction, in relation to time for (a) Pd/GPTMS, (b) Pd/EETMS, (c) Pd/GO/GPTMS, and (d) Pd/GO/EETMS. Inset to graph (d) shows, kinetics of the process. (III) Absorption spectra of reduction of p-nitrophenol using heat treated catalyst (a) at 423 K and (b) 623 K and corresponding bar diagrams (b) and (d). (IV) (a) and (b) Stability test before and after 5–6 days, (c) and (d) represent the variation in absorbance relative to time (e) recyclability assessment over 5 experimental cycles for the silica alginate beads entrapped with nanocomposites. Stability and recyclability was examined through p-nitroaniline reduction with 1.19 M hydrazine.

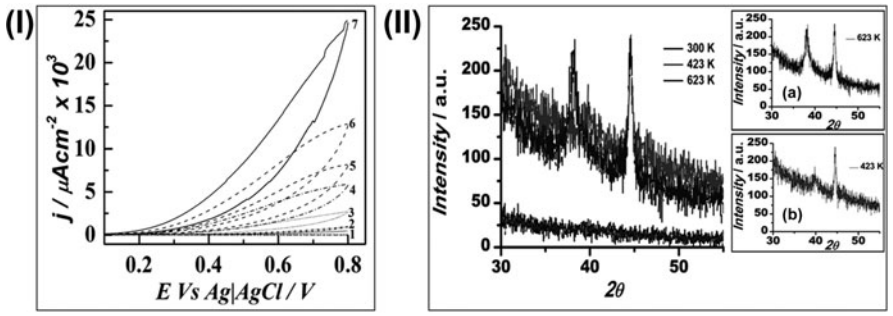


FIG. 7. (I) Cyclic voltammograms of blank (1) in absence and the presence of 50 mM hydrazine; blank (2), Pd/GPTMS (3), Pd/EETMS (4), Pd/GO/EETMS (5), Pd/GO/GPTMS (6) and Pd/GO/EETMS (7) at 423 and 623 K in phosphate buffer pH 7.0 containing 0.5 M KCl. (II) XRD patterns of silica beads at room temperature and after treating at elevated temperatures, (a) at 623 and (b) 423 K.

The silica alginate beads with Pd/GO/EETMS, the most efficient catalyst as reported from the investigations carried out, are used at high temperatures (up to 630 K), and examined for their catalytic activity. Treating with elevated temperatures, tailored the properties, for instance, the crystallinity of the material enhanced[43] to

https://doi.org/10.1557/jmr.2017.226 Published online by Cambridge University Press

a much higher extent which is clearly visible from the X-ray diffractograms shown in Fig. 7(II).

The modified material responds even more faster toward the decomposition of hydrazine (Fig. 4), conversion of MB to leucoMB, reduction of *p*-nitroaniline to *p*-diaminobenzene [Fig. 6(III)] and electrochemical oxidation of hydrazine as shown in Fig. 7(I).

IV. CONCLUSION

To summarize, we have reported the novel and highly effective methodology to fabricate mesoporous silica alginate beads with precisely controlled pore sizes (2–10 nm). These nanoparticles are endowed with exceptionally tunable properties essential for their utilization in heterogeneous catalytic reactions specifically for the hydrogen evolution from the decomposition of hydrazine. Out of different systems (silica beads encapsulated with Pd/GPTMS, Pd/EETMS, Pd/GO/GPTMS, and Pd/GO/EETMS), one with Pd/GO/EETMS nanoparticles, is found to be highly active material, justifying the role of alkoxysilane in improving the properties of the materials. When treated at elevated temperatures, silica beads with Pd/GO/EETMS nanoparticles required mesoporous frame-up with raised crystallinity and are found to exhibit the highest level activity, when explored for the catalytic potential. This miniatured machinery can be reliably adopted in various other applications.

ACKNOWLEDGMENT

Financial assistance to Indian Institute of Technology (BHU) is greatly acknowledged for the support of Institute Project No. IPR/2016-17/4299.

REFERENCES

1. X. Li, J. Yu, J. Low, Y. Fang, J. Xiaoc, and X. Chen: Engineering heterogeneous semiconductors for solar water splitting. *J. Mater. Chem. A* **3**, 2485–2534 (2015).
2. X. Chen, S. Shen, L. Guo, and S.S. Mao: Semiconductor-based photocatalytic hydrogen generation. *Chem. Rev.* **110**, 6503–6570 (2010).
3. X. Chen, C. Li, M. Grätzel, R. Kosteckid, and S.S. Mao: Nanomaterials for renewable energy production and storage. *Chem. Soc. Rev.* **41**, 7909–7937 (2012).
4. S.K. Singh and Q. Xu: Nanocatalysts for hydrogen generation from hydrazine. *Catal. Sci. Technol.* **3**, 1889–1900 (2013).
5. S.I. Orimo, Y. Nakamori, R.E. Jennifer, A. Zuttel, and C.M. Jensen: Complex hydrides for hydrogen storage. *Chem. Rev.* **107**, 4111–4132 (2007).
6. M. Yadav and Q. Xu: Liquid-phase chemical hydrogen storage materials. *Energy Environ. Sci.* **5**, 9698–9725 (2012).
7. M. Zheng, R. Cheng, X. Chen, N. Li, L. Li, X. Wang, and T. Zhang: A novel approach for CO-free H_2 production via catalytic decomposition of hydrazine. *Int. J. Hydrogen Energy* **30**, 1081–1089 (2005).
8. S.K. Singh, A.K. Singh, K. Aranishi, and Q. Xu: Noble-metal-free bimetallic nanoparticle-catalyzed selective hydrogen generation from hydrous hydrazine for chemical hydrogen storage. *J. Am. Chem. Soc.* **133**, 19638–19641 (2011).
9. S.K. Singh, X.B. Zhang, and Q. Xu: Room-temperature hydrogen generation from hydrous hydrazine for chemical hydrogen storage. *J. Am. Chem. Soc.* **131**, 9894–9895 (2009).
10. L.J. Liu, U. Burghaus, F. Besenbacher, and Z.L. Wang: Preparation and characterization of nanomaterials for sustainable energy production. *ACS Nano* **4**, 5517–5526 (2010).
11. C.E. Bunker and M.J. Smith: Nanoparticles for hydrogen generation. *J. Mater. Chem.* **21**, 12173–12180 (2011).
12. K.V. Manukyan, A. Cros, S. Rouvimov, J. Miller, A.S. Mukasyan, and E.E. Wolf: Low temperature decomposition of hydrous hydrazine over FeNi/Cu nanoparticles. *Appl. Catal., A* **476**, 47–53 (2014).
13. S.N. Oliaee, C. Zhang, S.Y. Hwang, H.M. Cheung, and Z. Peng: Hydrogen production via hydrazine decomposition on model platinum–nickel nanocatalyst with a single (111) facet. *J. Phys. Chem. C* **120**, 9764–9772 (2016).
14. S.K. Singh and Q. Xu: Complete conversion of hydrous hydrazine to hydrogen at room temperature for chemical hydrogen storage. *J. Am. Chem. Soc.* **131**, 18032–18033 (2009).
15. J. Wang, X-B. Zhang, Z-L. Wang, L-M. Wang, and Y. Zhang: Rhodium–nickel nanoparticles grown on graphene as highly efficient catalyst for complete decomposition of hydrous hydrazine at room temperature for chemical hydrogen storage. *Energy Environ. Sci.* **5**, 6885–6888 (2012).
16. X. Yang, X. Zhang, Y. Ma, Y. Huang, Y. Wang, and Y. Chen: Superparamagnetic graphene oxide–Fe_3O_4 nanoparticles hybrid for controlled targeted drug carriers. *J. Mater. Chem.* **19**, 2710–2714 (2009).
17. Y. Choi, H.S. Bae, E. Seo, S. Jang, K.H. Park, and B.S. Kim: Hybrid gold nanoparticle-reduced graphene oxide nanosheets as active catalysts for highly efficient reduction of nitroarenes. *J. Mater. Chem.* **21**, 15431–15436 (2011).
18. Y.K. Kim, S.W. Han, and D.H. Min: Graphene oxide sheath on Ag nanoparticle/graphene hybrid films as an antioxidative coating and enhancer of surface-enhanced Raman scattering. *ACS Appl. Mater. Interfaces* **4**, 6545–6551 (2012).
19. A.N. Bezbaruah, S. Krajangpan, B.J. Chisholm, E. Khan, and J.J. Elorza Bermudez: Entrapment of iron nanoparticles in calcium alginate beads for groundwater remediation applications. *J. Hazard. Mater.* **166**, 1339–1343 (2009).
20. H. Kim, H.J. Hong, J. Jung, S.H. Kim, and J.W. Yang: Degradation of trichloroethylene (TCE) by nanoscale zero-valent iron (nZVI) immobilized in alginate bead. *J. Hazard. Mater.* **176**, 1038–1043 (2010).
21. P. Pankongadisak, U.R. Ruktanonchai, P. Supaphol, and O. Suwantong: Preparation and characterization of silver nanoparticles-loaded calcium alginate beads embedded in gelatin scaffolds. *AAPS PharmSciTech* **15**, 1105–1115 (2014).
22. Y. Kuang, D. Jianhua, R. Zhou, Z. Chen, M. Megharaj, and R. Naidu: Calcium alginate encapsulated Ni/Fe nanoparticles beads for simultaneous removal of Cu (II) and monochlorobenzene. *J. Colloid Interface Sci.* **447**, 85–91 (2015).
23. J. Klein, J. Stock, and K.D. Vorlop: Pore size and properties of spherical Ca-alginate biocatalysts. *Eur. J. Appl. Microbiol. Biotechnol.* **18**, 86–91 (1983).
24. D. Brunel, A. Cauvel, F.D. Renzo, F. Fajula, B. Fubini, B. Onida, and E. Garrone: Preferential grafting of alkoxysilane coupling agents on the hydrophobic portion of the surface of micelle-templated silica. *New J. Chem.* **24**, 807–813 (2000).
25. P.C. Pandey and R. Singh: Tetrahydrofuran hydroperoxide and 3-aminopropyl trimethoxysilane mediated controlled synthesis of Pd, Pd–Au, Au–Pd nanoparticles: Role of palladium nanoparticles on the redox electrochemistry of ferrocene monocarboxylic acid. *Electrochim. Acta* **138**, 163–173 (2014).

https://doi.org/10.1557/jmr.2017.226 Published online by Cambridge University Press

26. P.C. Pandey and G. Pandey: One-pot two-step rapid synthesis of 3-aminopropyltrimethoxysilane-mediated highly catalytic Ag@(PdAu) trimetallic nanoparticles. *Catal. Sci. Technol.* **6**, 3911–3917 (2016).
27. P.C. Pandey, S. Shukla, and Y. Pandey: 3-aminopropyltrimethoxysilane and grapheneoxide/reduced graphene oxide-induced generation of gold nanoparticles and their nanocomposites: Electrocatalytic and kinetic activity. *RSC Adv.* **6**, 80549–80556 (2016).
28. P.C. Pandey and G. Pandey: Synthesis of gold nanoparticles resistant to pH and salt for biomedical applications; functional activity of organic amine. *J. Mater. Res.* **31**, 3313–3323 (2016).
29. S. Tafreshi, A. Roldanab, and H. Nora de Leeuw: Density functional theory calculations of the hydrazine decomposition mechanism on the planar and stepped Cu (111) surfaces. *Phys. Chem. Chem. Phys.* **17**, 21533–21546 (2015).
30. T. Seo, R. Kurokawa, and B. Sato: A convenient method for determining the concentration of hydrogen in water: Use of methylene blue with colloidal platinum. *Med. Gas Res.* **2**, 1 (2012). doi: 10.1186/2045-9912-2-1.
31. Z.D. Pozun, S.E. Rodenbusch, E. Keller, K. Tran, W. Tang, K.J. Stevenson, and G. Henkelman: A systematic investigation of *p*-nitrophenol reduction by bimetallic dendrimer encapsulated nanoparticles. *J. Phys. Chem. C* **117**, 7598–7604 (2013).
32. S. Gu, S. Wunder, Y. Lu, and M. Ballauff: Kinetic analysis of the catalytic reduction of 4-nitrophenol by metallic nanoparticles. *J. Phys. Chem. C* **118**, 18618–18625 (2014).
33. R. Zhang, Lu. Liu, Y. Li, W. Wang, R. Li: Electroxidation Kinetics of Hydrazine on Y-type Zeolite encapsulated Ni(II) (salen) Complex Supported on Graphite Modified Electrode. *Int. J. Electrochem. Sci.*, **10**, 2355–2369 (2015).
34. D.J. Darensbourg, J.L. Rodgers, and C.C. Fang: The copolymerization of carbon dioxide and [2-(3,4-epoxycyclohexyl)ethyl] trimethoxysilane catalyzed by (salen)CrCl. Formation of a CO_2 soluble polycarbonate. *Inorg. Chem.* **42**, 4498–4500 (2003).
35. J.I. Paredes, S. Villar-Rodil, A. Martínez-Alonso, and J.M.D. Tascón: Graphene oxide dispersions in organic solvents. *Langmuir* **24**, 10560–10564 (2008).
36. D. Konios, M.M. Stylianakis, E. Stratakis, and E. Kymakis: Dispersion behaviour of graphene oxide and reduced graphene oxide. *J. Colloid Interface Sci.* **430**, 108–112 (2014).
37. M. Pérez-Lorenzo: Palladium nanoparticles as efficient catalysts for Suzuki cross-coupling reactions. *J. Phys. Chem. Lett.* **3**, 167–174 (2012).
38. A. Krittayavathananon, P. Srimuk, S. Luanwuthi, and M. Sawangphruk: Palladium nanoparticles decorated on reduced graphene oxide rotating disk electrodes toward ultrasensitive hydrazine detection: Effects of particle size and hydrodynamic diffusion. *Anal. Chem.* **86**, 12272–12278 (2014).
39. X. Zhang, J. Zhu, C.S. Tiwary, Z. Ma, H. Huang, J. Zhang, Z. Lu, W. Huang, and Y. Wu: Palladium nanoparticles supported on nitrogen and sulfur dual-doped graphene as highly active electrocatalysts for formic acid and methanol oxidation. *ACS Appl. Mater. Interfaces* **8**, 10858–10865 (2016).
40. Y.X. Huang, J.F. Xie, X. Zhang, L. Xiong, and H.Q. Yu: Reduced graphene oxide supported palladium nanoparticles via photo-assisted citrate reduction for enhanced electrocatalytic activities. *ACS Appl. Mater. Interfaces* **6**, 15795–15801S (2014).
41. C.C. Kocak, A. Altın, B. Aslisen, and S. Kocak: Electrochemical preparation and characterization of gold and platinum nanoparticles modified poly(taurine) film electrode and its application to hydrazine determination. *Int. J. Electrochem. Sci.* **11**, 233–249 (2016).
42. K. Park, H.J. Yu, W.K. Chung, B.J. Kim, and S.H. Kim: Effect of heat-treatment on CdS and CdS/ZnS nanoparticles. *J. Mater. Sci.* **44**, 4315–4320 (2009).
43. K. Kuroda, T. Ishida, and M. Haruta: Reduction of 4-nitrophenol to 4-aminophenol over Au nanoparticles deposited on PMMA. *J. Mol. Catal.* **298**, 7–11 (2009).
44. S. Wunder, F. Polzer, Y. Lu, Y. Mei, and M. Ballauff: Kinetic analysis of catalytic reduction of 4-nitrophenol by metallic nanoparticles immobilized in spherical polyelectrolyte brushes. *J. Phys. Chem. C* **114**, 8814–8820 (2010).
45. C. Kastner and A.F. Thunemann: Catalytic reduction of 4-nitrophenol using silver nanoparticles with adjustable activity. *Langmuir* **32**, 7383–7391 (2016).

Supplementary Material

To view supplementary material for this article, please visit https://doi.org/10.1557/jmr.2017.226.

https://doi.org/10.1557/jmr.2017.226 Published online by Cambridge University Press